Eur. Phys. J. A **29**, 261–270 (2006)
DOI 10.1140/epja/i2005-10314-9

THE EUROPEAN PHYSICAL JOURNAL A

First measurements of the ^{16}O(e, e′pn)^{14}N reaction

D.G. Middleton[1,a], J.R.M. Annand[1], C. Barbieri[2], P. Barneo[3], H.P. Blok[3], R. Böhm[4], M.O. Distler[4], J. Friedrich[4], C. Giusti[5], D.I. Glazier[1], P. Grabmayr[6], T. Hehl[6], J. Heim[6], W.H.A. Hesselink[3,6], E. Jans[3], M. Kohl[4], L. Lapikás[3], I.J.D. MacGregor[1], I. Martin[6], J.C. McGeorge[1], H. Merkel[4], F. Moschini[6], G. Rosner[1], M. Seimetz[4], H. de Vries[3], Th. Walcher[4], D.P. Watts[1,8], and B. Zihlmann[3,7]

[1] Department of Physics and Astronomy, University of Glasgow, Scotland, UK
[2] Gesellschaft für Schwerionenforschung, Planckstr. 1, 64291 Darmstadt, Germany
[3] NIKHEF, P.O. Box 41882, Amsterdam, The Netherlands
[4] Institut für Kernphysik, Universität Mainz, Germany
[5] Dipartimento di Fisica Nucleare e Teorica dell'Università degli Studi di Pavia and Istituto Nazionale di Fisica Nucleare, Sezione di Pavia, I-27100 Pavia, Italy
[6] Physikalisches Institut, Universität Tübingen, Germany
[7] Vrije Universiteit, Amsterdam, The Netherlands
[8] School of Physics, University of Edinburgh, Scotland, UK

Received: 20 December 2005 / Revised: 23 April 2006 /
Published online: 15 September 2006 – © Società Italiana di Fisica / Springer-Verlag 2006
Communicated by R. Milner

Abstract. This paper reports on the first measurement of the ^{16}O(e, e′pn)^{14}N reaction. Data were measured in kinematics centred on a super-parallel geometry at energy and momentum transfers of 215 MeV and 316 MeV/c. The experimental resolution was sufficient to distinguish groups of states in the residual nucleus but not good enough to separate individual states. The data show a strong dependence on missing momentum and this dependence appears to be different for two groups of states in the residual nucleus. Theoretical calculations of the reaction using the Pavia code do not reproduce the shape or the magnitude of the data.

PACS. 13.75.Cs Nucleon-nucleon interactions (including antinucleons, deuterons, etc.) – 21.30.Fe Forces in hadronic systems and effective interactions – 25.30.Fj Inelastic electron scattering to continuum

1 Introduction

It is generally accepted that independent particle models, in which nucleons move in a mean field, provide a good description of the structure of nuclei. However, it has been shown that it is necessary to include two-nucleon correlations beyond the mean field in order to describe some basic nuclear properties such as binding energy [1,2].

Further evidence of the effects of correlated two-nucleon behaviour comes from measurements of spectroscopic strengths for the knockout of protons from nuclei with $A > 4$ [3–5]. The average value of the measured spectroscopic strength for a range of nuclei was found to be $\approx$ 65% of that predicted by independent particle models. It was also found that the spectroscopic strength of the "normally empty" orbitals above the Fermi edge was non-zero. The observed depletion of the Fermi sea is, to a large extent, believed to be due to the influence of NN-correlations in the nucleus. These nucleon-nucleon correlations cause the promotion of nucleons to states above the Fermi level and generate large nucleon momenta within the nucleus.

Modern potentials describing the mutual interaction of nucleons contain many components, which are dependent on distance, spin and isospin of the nucleons, many of which are non-local. The potential at short distances is dominated by a strong scalar repulsive interaction, which prevents a nucleus from collapsing and which suppresses the uncorrelated nuclear wave function at small intranucleonic distances. These are the so-called short-range correlations (SRC). A possible way to account for the SRC is the introduction of defect (*i.e.*, suppression) functions for the radial wave functions, which are calculated for each partial wave by solving the Schrödinger equation for two bound nucleons within a model space that contains the high-momentum degrees of freedom and accounting for the Pauli-blocking effects of the remaining $A - 2$ nucle-

[a] *Present address:* Physikalisches Institut, Universität Tübingen, Germany;
e-mail: duncan@pit.physik.uni-tuebingen.de

ons [6,7]. It is predicted, that SRC contribute differently for different final states of the residual nucleus [8].

The second main component of NN-correlations is a tensor correlation (TC) term, which depends on the spin and spatial orientation of the two nucleons [1,9]. This term favours energetically the situation where the spins of neighbouring nucleons are aligned along their relative vector separation. These correlations are mainly due to the strong tensor components of the pion exchange contribution to the NN interaction and are very important in the wave function of a pn pair, but much less so for pp pairs [6].

Electromagnetically induced two-nucleon knockout is a powerful tool to investigate the role of correlated NN motion in the nucleus. A real or virtual photon, absorbed by one of the nucleons in a correlated pair which are subsequently ejected from the nucleus via one-body currents (SRC or TC), can provide information on the correlations between them [10–12]. In an interaction with the one-body nuclear current the (virtual) photon is absorbed by one nucleon of a correlated pair which is knocked out of the nucleus. This leaves the residual nucleus in an excited state and subsequently the second nucleon of the correlated pair is likely to be emitted from the nucleus.

Additional processes have to be taken into account when studying NN-knockout reactions. There are competing two-body mechanisms such as meson exchange currents (MEC) and isobar currents (IC) that contribute to the measured cross-section. Final-state interactions (FSI) between the outgoing nucleons and the residual nucleus and between the two outgoing nucleons also complicate the picture. The importance of the contribution to the cross-section of each of these other processes depends strongly on the reaction channel and hence studies of the (γ, pp), (γ, pn), $(\mathrm{e}, \mathrm{e'pp})$ and $(\mathrm{e}, \mathrm{e'pn})$ can greatly improve our understanding of the separate contributing mechanisms.

While NN-knockout experiments with real photons are only sensitive to transverse components of the interaction, virtual photons are sensitive to both the longitudinal and transverse components [12]. The longitudinal cross-section is dominated by one-body currents and is therefore more sensitive to NN-correlations. Electron scattering experiments therefore have significant advantages for investigating these properties. In contrast, two-body currents like IC and MEC are strongest in the transverse cross-section and are therefore more suitably studied with real photon beams [12].

Different properties of the nuclear response to virtual photons can be studied using $(\mathrm{e}, \mathrm{e'pp})$ and $(\mathrm{e}, \mathrm{e'pn})$ reactions. For the $(\mathrm{e}, \mathrm{e'pp})$ reaction SRC are expected to dominate the longitudinal response. For the $(\mathrm{e}, \mathrm{e'pn})$ reaction TC are expected to play a major role in the longitudinal nuclear response whereas SRC make a relatively minor contribution [13,7]. Moreover, the results of [6] and [7] suggest that TC influence the cross-section principally through the Delta current.

In general, two-body currents are more important in pn-knockout reactions than in pp-knockout [14]. The contribution from MEC to the $(\mathrm{e}, \mathrm{e'pp})$ cross-section is suppressed because the virtual photon will not couple to neutral pions. This is not the case for pn-knockout where MEC make a substantial contribution to the cross-section, particularly in the transverse part. IC can contribute substantially to the reaction cross-section for pn-knockout, their importance grows as the transferred photon energy approaches the Delta-resonance region. Again their contribution is more important in the transverse nuclear response.

FSI between the outgoing nucleons and the residual nucleus have often been treated theoretically using an optical model. However, it has been shown recently [15] that the mutual interaction between the two emitted nucleons can also have a large effect on reaction cross-sections. The magnitude of the effects depends strongly on the reaction channel and on the particular kinematics. For instance, an increase in the calculated $^{16}\mathrm{O}(\mathrm{e}, \mathrm{e'pp})$ cross-section by nearly an order of magnitude [15] has been found in super-parallel kinematics, where the two protons are emitted anti-parallel to one another, at large recoil momentum. In pn emission the effect is partially cancelled by destructive interference with the pion seagull MEC term [16].

The first electron scattering study of NN-knockout was a measurement of the $^{12}\mathrm{C}(\mathrm{e}, \mathrm{e'pp})$ reaction at NIKHEF [17,18]. This experiment measured two-proton knockout at an energy transfer $\omega = 212$ MeV and a three-momentum transfer $|\mathbf{q}| = 270\,\mathrm{MeV}/c$. The measured missing energy spectrum shows a signature for knockout of proton pairs from $(1\mathrm{p})^2$, $(1\mathrm{p}, 1\mathrm{s})$, and $(1\mathrm{s})^2$ states. The data were compared with a direct-knockout calculation which includes one- and two-body currents. This comparison shows that the measured cross-section for the knockout of a $(1\mathrm{p})^2$ pair can largely be attributed to SRC.

Measurements at NIKHEF of the $^{16}\mathrm{O}(\mathrm{e}, \mathrm{e'pp})$ reaction [19,20] using large solid-angle proton detectors were able to separate the ground state in the residual $^{14}\mathrm{C}$ nucleus. Clear signatures of SRC were observed in transitions to this state. A further NIKHEF measurement [21] also obtained experimental evidence for SRC from the measured energy-transfer dependence of the $^{16}\mathrm{O}(\mathrm{e}, \mathrm{e'pp})^{14}\mathrm{C}_{g.s.}$ reaction. This earlier evidence of SRC has received further confirmation in recent $(\mathrm{e}, \mathrm{e'p})$ experiments at JLab [22].

Similar results from the $^{16}\mathrm{O}(\mathrm{e}, \mathrm{e'pp})$ reaction were obtained with the three-spectrometer setup at the Mainz Microtron MAMI [23]. These measurements were carried out in super-parallel kinematics and various low-lying states in $^{14}\mathrm{C}$ were populated. Comparison with theoretical calculations [24] provided evidence that SRC affect nucleon pairs with small centre-of-mass momentum in relative S-states.

The $(\mathrm{e}, \mathrm{e'pp})$ reaction has also been measured over a wide range of kinematics in the $^3\mathrm{He}$ nucleus [25]. At a momentum transfer of $\mathbf{q} = 375\,\mathrm{MeV}/c$ data were taken at transferred energies ranging from 170 to 290 MeV and at $\omega = 220\,\mathrm{MeV}$, measurements were performed at $\mathbf{q} =$ 305, 375, and $445\,\mathrm{MeV}/c$. The data are compared with continuum-Faddeev calculations, which indicate that at $\omega = 220\,\mathrm{MeV}$ and for neutron momenta below $100\,\mathrm{MeV}/c$, the cross-section is dominated by direct two-proton emis-

sion induced by a one-body hadronic current. At higher neutron momenta deviations between the data and calculations are attributed to additional contributions from isobar currents.

There have been several measurements of real-photon two-nucleon knockout reactions on ^{16}O [26–28]. The first measurement [26], carried out at the Mainz 180 MeV electron Microtron MAMI-A, measured both reaction channels and covered the photon energy range 80–131 MeV. The energy resolution of 7 MeV was too poor to resolve the different excited states within the residual ^{14}N nucleus. However, it was observed that the strength of the (γ, pp) cross-section for the emission of $(1\mathrm{p})^2$ nucleon pairs was very small and amounted to only $\approx 2\%$ of the corresponding (γ, pn) cross-section.

The study of ref. [27] measured the ^{16}O(γ, pn) reaction at $E_\gamma = 72$ MeV. An energy resolution of better than 2 MeV was achieved which allowed cross-sections for the excitation of individual excited states in ^{14}N to be measured. The ground (1^+), 3.95 MeV (1^+) and 7.03 MeV (2^+) states were all observed, but there was no excitation of the 2.3 MeV (0^+) state. Comparison was made with theoretical calculations including MEC and IC. The calculated cross-sections significantly underestimated the strength of all the observed excited states but did predict the 3.95 MeV (1^+) state would be strongly excited, as observed. It was deduced that states with CM pair orbital angular momenta $L = 0$ and $L = 2$ both contributed strongly to the observed spectrum, and the absence of the 2.3 MeV (0^+) state was attributed to the dominance of interactions with ^{3}S$_1$ pn pairs as assumed in the basic quasi-deuteron process.

A further study of the ^{16}O(γ, pn) reaction [28] was carried out for the photon energy range $E_\gamma = 98.5$ to 141.0 MeV with an energy resolution of 2.8 MeV. Protons were detected at two angles: 76° and 82° with coincident neutrons being detected at corresponding quasi-deuteron angles. Only the 3.95 MeV (1^+) state in the residual ^{14}N nucleus was significantly populated. This state is expected to have a large $L = 0$ component compared to the other two states seen in the previous experiment [27] which both have strong $L = 2$ components. The low recoil momentum range sampled in [28] therefore favoured excitation of the 3.95 MeV (1^+) state.

In the present paper we report the results of the first measurements of the ^{16}O(e, e′pn)^{14}N reaction. The experiment was performed at the University of Mainz 855 MeV electron microtron MAMI. The data were centred on super-parallel kinematics similar to those used in a previous ^{16}O(e, e′pp) measurement [23], also carried out at MAMI.

2 Theoretical framework

In exclusive two-nucleon knockout electron scattering experiments energy and momentum are transferred to a nucleus by a virtual photon and the momenta of the scattered electron and both nucleons are determined. Only processes where the recoil nucleus is left intact and no secondary particles are created are considered here.

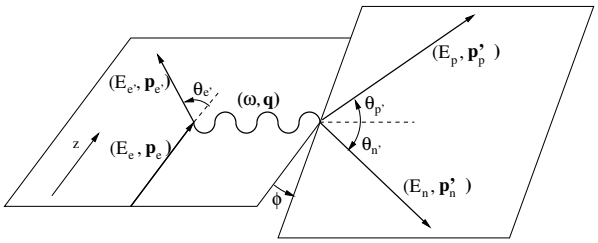

Fig. 1. Schematic of the kinematics for a two-nucleon knockout reaction.

2.1 Kinematics of the reaction

The kinematics for the ^{16}O(e, e′pn)^{14}N reaction are shown schematically in fig. 1. In the one-photon exchange approximation, the transferred virtual photon has an energy $\omega = E_e - E_{e'}$ and three-momentum $\mathbf{q} = \mathbf{p}_e - \mathbf{p}_{e'}$ where the subscripts e and e′ represent the incident and scattered electron, respectively. The proton and neutron are ejected from the ^{16}O nucleus with momenta $\mathbf{p}'_p$ and $\mathbf{p}'_n$ and are detected in coincidence with the scattered electron. In the present experiment the data were centred on a super-parallel kinematic setting where the proton is emitted in the forward direction parallel to the direction of $\mathbf{q}$ and the neutron is emitted anti-parallel to $\mathbf{q}$.

In an exclusive ^{16}O(e, e′pn)^{14}N reaction the final state can be completely reconstructed using the missing momentum

$$\mathbf{p}_m = \mathbf{q} - \mathbf{p}'_p - \mathbf{p}'_n = \mathbf{p}_r \tag{1}$$

which is equal to the momentum of the undetected ^{14}N recoil nucleus $\mathbf{p}_r$. Using a non-relativistic approximation, the missing energy (E_m) can be defined as

$$E_m = \omega - T_p - T_n - T_r = S_{pn} + E_x, \tag{2}$$

where T_p, T_n and T_r are the kinetic energies of the proton, neutron and recoil nucleus, respectively; T_r can be determined from $\mathbf{p}_r$. The ^{14}N nucleus can be left in a variety of states with excitation energy, E_x. S_{pn} is the separation energy for the reaction.

The ^{2}H(e, e′pn) reaction, used for calibration purposes, is over-determined because both emitted particles were detected in the final state and there is no residual nucleus. The missing energy is defined as

$$E_m = \omega - T_p - T_n \tag{3}$$

in this case.

2.2 Theoretical calculations

To help interpret the experimental data we compare the results to the microscopic calculations of Giusti *et al.* described in refs. [7,29] with improvements to the model

Table 1. The kinematical settings for which theoretical calculations were performed. θ_{pq} and θ_{pn} are the angles subtended by the trajectories of the proton and virtual photon and the proton and neutron, respectively.

Setting	ω [MeV]	q [MeV/c]	$\theta_{e'}$ [°]	θ_{pq} [°]	θ_{pn} [°]
1	245	333	18	6	165
2	185	300	18	6	165
3	215	316	18	2	165
4	215	316	18	8	165
5	215	316	18	6	155
6	215	316	18	6	175

described in ref. [6]. These were performed for a number of kinematical settings covering the energy ranges and angular ranges subtended by the experimental set-up and the average cross-section was used for comparison to the data. Table 1 shows the settings for which the calculations were performed.

In the calculations the transition amplitude for the exclusive (e, e′pn) knockout reaction contains contributions from both one-body and two-body hadronic currents. The one-body current contains the longitudinal charge term and the transverse convection and spin terms. The two-body current is derived performing a non-relativistic reduction of the lowest-order Feynman diagrams with one-pion exchange. Therefore currents corresponding to the seagull and pion-in-flight diagrams and to the diagrams with intermediate Delta-isobar configurations are included [7,29].

The final-state wave function includes the interaction of each one of the two outgoing nucleons with the residual nucleus, that is treated with a complex phenomenological optical potential containing central, Coulomb and spin-orbit terms. The mutual interaction of the two ejected nucleons is not included in the calculations. Although the effect of NN-FSI is non-negligible for the (e, e′pn) cross-section, quantitative effects are small and the qualitative features of the theoretical results are basically the same [16].

In the initial state the two-nucleon overlap function between the ground state of the target and the final state of the residual nucleus has been computed partitioning the Hilbert space, in order to determine the contribution of long-range correlation (LRC) and SRC separately. The LRC, describing the collective motion at low energy as well as the long-range part of TC, were computed using the self-consistent Green's function (SCGF) formalism [2] in an appropriate harmonic-oscillator basis. The effects of SRC due to the central and tensor part at high momenta were added by computing the appropriate defect functions. A crucial contribution is given here by TC, which produce defect functions also for channels for which the uncorrelated wave function vanishes. This partitioning process is justified by the separation of the momentum scales associated to SRC and LRC. The Bonn-C interaction [30] was used in the calculations.

3 Experimental set-up

The measurements were performed using the electron scattering facility (3-spectrometer facility) of the 100% duty factor Mainz Microtron MAMI [31]. The 855 MeV, 10–20 μA electron beam was incident on a waterfall target [32] of thickness 74 mg cm^{-2}. A deuterium target [33, 34] was used for detector calibration. This target set-up consisted of a cylindrical cell containing liquid ^{2}H with a nominal thickness of 165 mg cm^{-2}. Beam currents of 0.25, 0.5 and 1 μA were used for calibration.

For both targets the scattered electrons were detected in Spectrometer B [35] which was placed at forward angles with respect to the beam, see table 2 and figs. 2 and 3. Spectrometer B is a magnetic spectrometer which has a solid angle of $\Delta\Omega = 5.6$ msr and momentum acceptance of $\Delta p/p = 15\%$, momentum resolution of $\delta p/p \leq 10^{-4}$ and angular resolution of $\delta\theta = \delta\phi = 1.5$ mrad.

To detect protons the Spectrometer A [35] was used with the ^{16}O target and the HADRON3 (H3) detector [36] from NIKHEF with the ^{2}H target. Again these were both placed at forward angles with respect to the beam but on the opposite side of the Spectrometer B, thus parallel to **q**. The Spectrometer A is a large-acceptance magnetic spectrometer with solid angle $\Delta\Omega = 28$ msr and momentum acceptance $\Delta p/p = 20\%$; the momentum and angular resolutions are the same as those of Spectrometer B. H3 is a large solid-angle ($\Delta\Omega = 230$ msr) hodoscope consisting of 128 bars of plastic scintillator divided into eight layers; two hodoscope layers and six energy determining layers. H3's proton energy acceptance range is 70–225 MeV. The energy resolution of H3 is 2.7% and the angular resolution is $\delta\theta = 0.52°$ and $\delta\phi = 1.04°$.

The Glasgow-Tübingen time-of-flight (TOF) detector system [37] was used for detection of neutrons for both targets. The TOF detector system consists of 96 bars of plastic scintillator, 72 of which are 5 cm thick "TOF" bars for neutron detection behind 24 "Veto" detectors, each 1 cm thick, used to discriminate between charged and neutral particles. The bars were arranged in three separate stands which were placed at backward angles with respect to the electron beam on the same side as Spectrometer B and so anti-parallel to **q**. Each stand consisted of 3 layers of 8 TOF bars which were positioned behind a layer of 8 overlapping Veto detectors. The position and timing resolutions of the TOF bars (FWHM) are $\leq$ 6 cm and $\leq$ 0.4 ns, respectively. The TOF stands were positioned at a distance of $\approx$ 7.5 m from the target giving angular resolutions of $\delta\theta = 1.5°$ and $\delta\phi = 0.5°$. For the detected

Table 2. Overview of the kinematic configurations for each target. The subscript e′, p and n$(1, 2, 3)$ represent the central position in the experimental hall of the electron and proton detectors and the three neutron detector stands, respectively. The incident beam energy was 855 MeV.

Target	ω [MeV]	q [MeV/c]	$\theta_{e'}$ [°]	θ_p [°]	θ_{n1} [°]	θ_{n2} [°]	θ_{n3} [°]
^{16}O	215	316	18	−38.8	120	136.5	155.5
^{2}H	190	300	15.5	−44	97	117	137

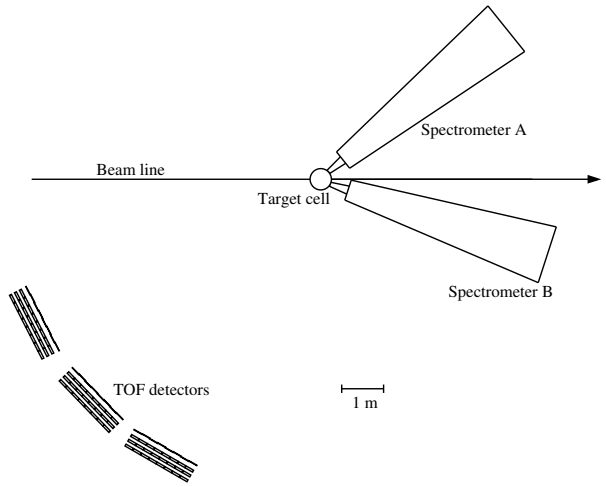

Fig. 2. Diagram of the detector set-up for the ^{16}O(e, e′pn) experiment using the waterfall target.

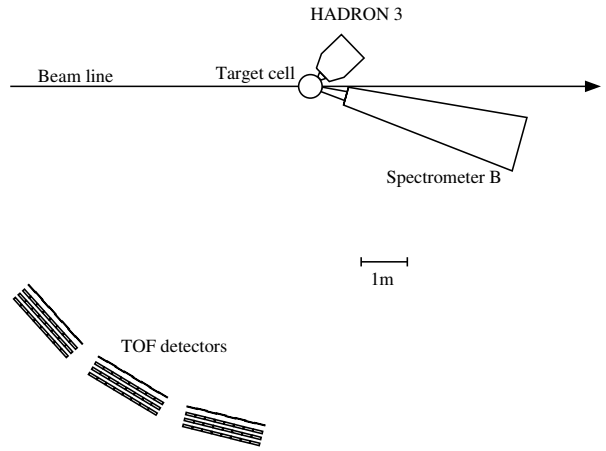

Fig. 3. Diagram of the detector set-up for the calibration runs using the ^{2}H cryogenic target.

neutron energy range of 30 to roughly 65 MeV an average energy resolution of ≈ 2 MeV (FWHM) was achieved. The neutron energy threshold was set in the analysis software at 30 MeV (see sect. 4.2).

To detect reactions involving the particles of interest coincidence-electronics were used. Each of the three detectors involved (Spectrometer B, H3/Spectrometer A and TOF) generated a signal on the detection of a particle meeting detector-specific requirements. In the set-up used here only an electron-proton coincidence was required to trigger an event read-out; the TOF detector systems were started when an electron was detected in Spectrometer B. TDCs provided the relative time information which was used to determine whether an event was in the threefold or twofold coincidence region or was completely random (see sect. 4.3).

4 Analysis

Using established procedures [35,36] the momenta of the scattered electron and emitted proton were determined. The energy of the emitted neutron was determined from its time of flight as described below. For each detector used in the experiment the arrival time of trigger signals was measured when a particle was detected and later corrected offline for time-of-flight differences and detector specific delays. This allowed real event coincidence times to be determined and prompt and random regions to be defined for subtraction of random coincidence events.

4.1 t_0 determination

To determine the energy and momentum of the emitted neutron an accurate measurement of the flight time from the reaction vertex to the position of detection within the TOF detector is required. The uncalibrated measured flight time contains contributions from delays caused by signal processing in the TOF detector. The effect of all such delays is referred to as the "t_0" value which must be subtracted to determine real neutron flight times.

In the experiment the start time for the TOF detectors was given by Spectrometer B. Corrections for delays in Spectrometer B were made so that the start time was that from when the reaction took place within the target cell. This was possible since the particle flight-time calibrations and offsets in Spectrometer B had been determined previously [35]. Any further delays were then only from the TOF system. The t_0 value for each TOF bar was determined using data from the highly overdetermined ^{2}H(e, e′pn) reaction. For each event the energy and momentum of the virtual photon were determined from the known incident beam energy and the angle and momentum of the scattered electron measured in Spectrometer B. Then using the measured polar and azimuthal angles of the neutron in TOF together with conservation of energy and momentum it is possible to evaluate the neutron energy and expected time of flight. When this expected flight time was subtracted from the measured flight time in TOF a constant offset, the t_0, was left for all real neutron events while random coincidences were spread over the measured time range. The mean values of the peaks were determined to obtain t_0 values for each of the TOF bars.

4.2 Determination of the neutron detection efficiency

While the detection efficiency of the electron and proton spectrometers is close to unity [35] the detection efficiency for neutrons in plastic scintillator is much lower, being $\approx 1\%$/cm.

The method employed to determine the neutron detection efficiency was by use of a Monte Carlo simulation developed by Stanton [38] and later improved by Cecil *et al.* [39]. This code calculates the neutron detection efficiency as a function of neutron kinetic energy and the detector threshold and a given detector material and geometry. Known cross-sections for most of the possible neutron reaction channels are included to give an overall reaction cross-section for a neutron traversing the scintillator

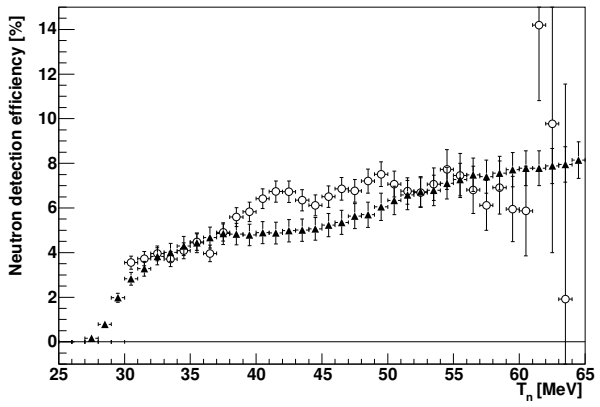

Fig. 4. Experimental neutron detection efficiency in the TOF detector system (circles) compared to that predicted by the Stanton code (triangles) [39].

material. The output of the code has been tested against measurements of the neutron detection efficiency for various types of plastic scintillator and detector dimensions and was found to be accurate to within about 10% [39].

A global software threshold was applied to the experimental data and the value of this threshold was applied to the Stanton code. The threshold energy was calibrated using proton energy deposition from consecutive TOF layers [37], and applied to the geometric mean of the pulse height recorded at both ends of the TOF bars. It was set above the effective hardware threshold so that it was independent of position. The threshold used was 20 $\mathrm{MeV}_{ee} \equiv 30\,\mathrm{MeV}$ neutron energy.

To model the efficiency of stands of three TOF layers, the detection efficiency for a bar in the second TOF layer was approximated by $\varepsilon\phi_\mathrm{r}$ where ε is the detection efficiency for one bar and ϕ_r is equal to $(1-\varepsilon)$ which approximately accounts for the reduction in neutron flux reaching the second layer. Similarly, a bar in the third layer is taken to have efficiency $\varepsilon\phi_\mathrm{r}^2$. The overall detection efficiency for the three layers was then the sum of the efficiencies for each individual layer. Any broken TOF bars in a set of three were not included in the overall efficiency although their effect on the neutron flux was still included.

To test the validity of the model of the neutron detection efficiency described above a comparison was made between the modelled efficiency using the Stanton code and the experimentally measured efficiency [40].

To do this the ratio of yield from the $^2\mathrm{H}(\mathrm{e},\mathrm{e}'\mathrm{pn})$ reaction to the yield from the $^2\mathrm{H}(\mathrm{e},\mathrm{e}'\mathrm{p})\mathrm{n}$ reaction, where the recoil neutron would have been above threshold in TOF, was determined. Data from all the separate TOF bars have been added to obtain this ratio. The comparison between this measured neutron detection efficiency in TOF and that predicted by the Stanton code model is shown in fig. 4.

The modelled efficiency was found to show fairly good agreement to the measured efficiency for neutron energies of 30–40 MeV but under-predicted the measurements by an average of $\approx 20\%$ for neutrons in the range 40–50 MeV. The deuterium data used for this comparison were taken when H3 was used for detection of the proton. It is believed that the structure seen in the measured efficiency between 40 and 50 MeV is due, in part, to the layering of the H3 detector. At the boundaries between scintillator layers the energy of some events is incorrectly determined because of pulsheight thresholds.

With the ^{16}O set-up the range of detected neutron energies was greater than that for the ^{2}H target, 30 to ≤ 130 MeV, so the efficiency model of three TOF bars employing the Stanton code was used. For the range of neutron energies where it was possible to make a reasonable comparison, 30–60 MeV, it was found that the Stanton code under-predicted the measured data by an average of $(13\pm2)\%$. Therefore, the efficiency taken from the Stanton code was increased universally by 13% for the evaluation of the cross-sections.

4.3 Random subtraction

In a triple coincidence experiment besides true triple coincidence events, various types of random coincidence events are also detected. These random events have to be subtracted from the experimental yield. The missing energy plot for this experiment before the subtraction of random events is shown in fig. 5 which also shows the contributions due to the different types of random coincidence events. The solid line, labelled $N_{e'pn}$, shows the observed triple coincidence events, the dashed line, labelled $N_{e'p}$, shows the contribution from true electron-proton coincidences with a random neutron, the dotted line, labelled $N_{(e'n)+(pn)}$, shows the contribution from events with true electron-neutron or true proton-neutron coincidences with the third particle being random and the dot-dashed line, labelled N_s, is from events where all three particles are in

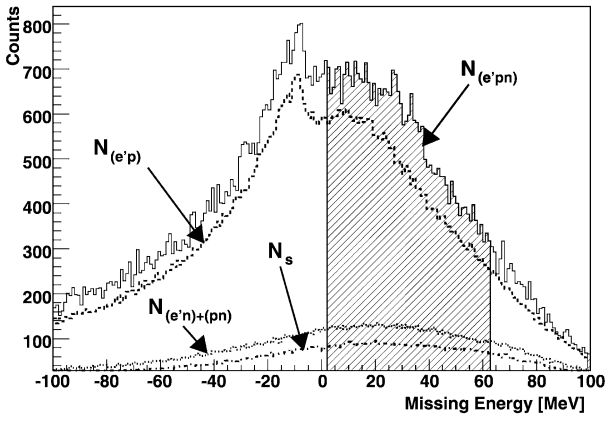

Fig. 5. Missing energy plot showing the contributions from the different types of random coincidences. The solid line, labelled $N_{e'pn}$, represents the observed triple coincidence events; the dashed line, labelled $N_{e'p}$, represents random neutron events; the dotted line, labelled $N_{(e'n)+(pn)}$, represents random proton and random electron events and the dot-dashed, labelled N_s, line represents events where all three detected particles are in random coincidence. The hatched area shows the E_m region covered in the excitation energy spectra of figs. 6 and 10.

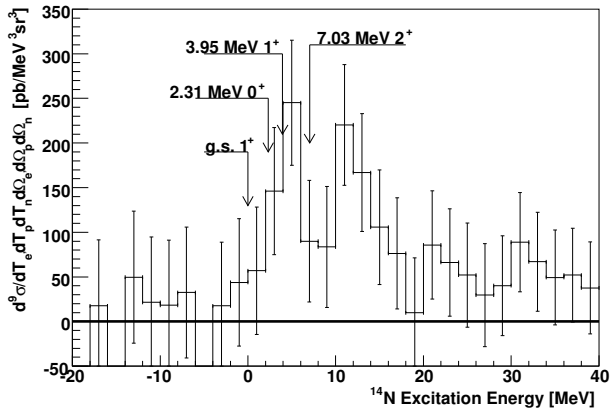

Fig. 6. Excitation energy of the residual ^{14}N nucleus after correction for random coincidences. The positions of the four lowest states in the ^{14}N are shown.

random coincidence. The hatched area indicates the E_m region covered in the excitation energy spectra of figs. 6 and 10.

As can clearly be seen in fig. 5 the largest contribution of random events was from those associated with a random neutron in the TOF detector. With the trigger used, when there was an acceptable electron-proton event, the TOF detectors were read out giving rise to the large number of random events covering the time window sampled.

The contributions from the different types of random events are determined from analysing data in different regions on a t_{e-p} *vs.* t_n plot, where t_{e-p} is the time difference between electron and proton detection and t_n is the neutron flight time. The arrival time distribution of random neutrons falls exponentially with increasing flight time [41]. This is because, with the QDC gates being controlled by the electron detector trigger, a particle from a nuclear reaction other than the one that triggered the electron detector can arrive earlier in time than the corresponding neutron. This particle can "steal" the QDC gate and the information pertaining to this second particle is processed by the detector instead. The chance of this happening falls exponentially with neutron flight time. To account for this a correction factor was applied to the random neutron events when performing the background subtraction: an exponential function was fitted to a region in the neutron flight time spectrum where only random events were expected and this was extended over the prompt-event region [40]. The ratio of number of events in the prompt region, determined using the fit, to that in the random region was then used as the correction factor. The factor f_c used was 1.037.

Having selected the regions to be used in the subtraction the number of prompt coincidences was determined using

$$True_{(e'pn)} = N_{(e'pn)} - f_c N_{(e'p)} - N_{(e'n)+(pn)} + f_c N_s, \quad (4)$$

where the subscript terms in brackets represent the different types of coincidence-event regions and the subscript s represents the threefold uncorrelated events; f_c is the correction factor applied to the random neutron events as described above. The addition of $f_c N_s$ corrects for the "extra" subtraction of 3-fold randoms included in the $f_c N_{(e'p)}$ term. In the (e′p) and (s) samples the neutron flight times were reassigned to be within the prompt neutron time region in order to determine the correct neutron energies. The time ranges covered by the TDCs was insufficient to obtain separate samples of the (e′n) and (pn) regions so these two contributions were treated as if they were all (e′n) events. Analysing the joint (e′n) and (pn) as (pn) events was also tried but this made no appreciable difference to the final results, the large random neutron contribution dominating the subtraction.

After the subtraction procedure is carried out real (e, e′pn) coincidence events are left, as shown in the ^{14}N excitation spectrum of fig. 6. The peak at ≈ 4 MeV corresponds to the position expected for the 3.95 MeV (1^+) state. A range of other states are observed in ^{14}N at $E_x \geq 9$ MeV. This is discussed further in the results section

4.4 Determination of cross-sections

The cross-section for a given kinematic variable X (*e.g.*, p_m) is determined in the following way:

$$\frac{\mathrm{d}^8\sigma}{\mathrm{d}V^8}(X) = \int_{E_x} \frac{N(X)}{\int \mathcal{L}\mathrm{d}t\mathcal{V}(X)} \left|\frac{\delta T_2}{\delta E_x}\right| \mathrm{d}E_x\,, \quad (5)$$

where $N(X)$ represents the number of true (e, e′pn) events for a given excitation energy range, $\int \mathcal{L}\mathrm{d}t$ is the integrated luminosity and $\mathcal{V}(X)$ is the experimental detection volume in phase space. The factor $|\delta T_2/\delta E_x|$ is a Jacobian where T_2, in this case, is the neutron kinetic energy and E_x is the missing energy range over which events are integrated.

The detection volume is calculated using a Monte Carlo method with a nine-dimensional volume $\mathcal{V}$ [42]. It takes into account the energy and angular acceptances of each of the detectors involved in the experiment. The neutron detection efficiency of the TOF detector system was included as a weight for events generated with the Monte Carlo method.

In electron scattering experiments the electron of interest can radiate photons reducing the energy of the incoming or scattered electron. This is usually evident in reconstructed missing energy spectra by the presence of a radiative tail, an example of which can be seen in fig. 7. The Monte Carlo program used to determine the detection volume includes multi-step radiative corrections following the formulæ of Mo and Tsai [43] to account for this.

4.5 Energy resolution

The energy resolution of the apparatus determined from calibration ^{2}H(e, e′pn) data taken when H3 was used for detection of the emitted proton. As the energy resolution of Spectrometer A is better than that of H3 this procedure only provides an upper limit of the energy resolution for the ^{16}O(e, e′pn) experiment.

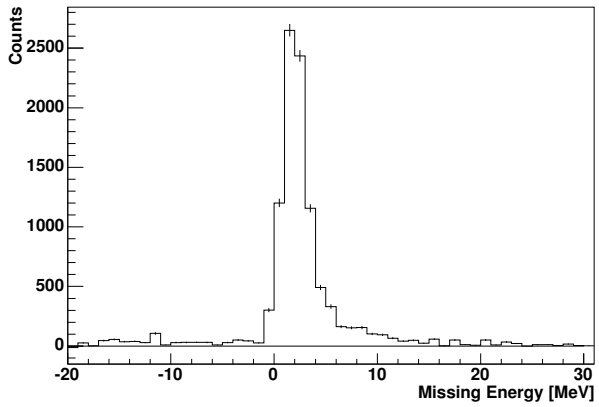

Fig. 7. Missing energy distribution for the ^{2}H(e, e′pn) reaction. The peak has a mean of 2.1 MeV and the resolution amounts to 3.0 MeV (FWHM).

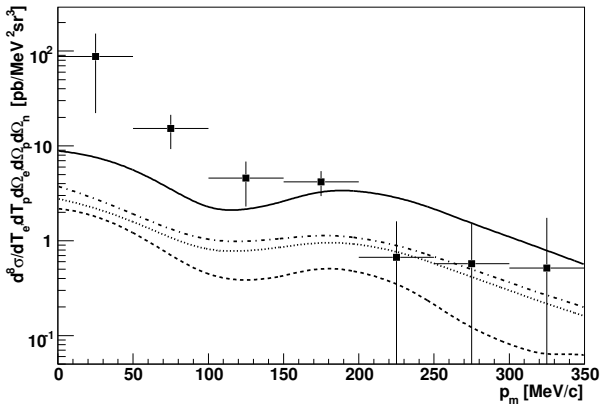

Fig. 8. Cross-section for events in the range $2 \leq E_x \leq 9$ MeV compared to calculations of the Pavia group. Calculations for transitions to the first three excited states, 3.95 MeV (1^+), 2.31 MeV (0^+) and 7.03 (2^+) are included in the calculations. The dashed line shows the cross-section for the one-body part of the reaction only; the dotted line also includes the π-seagull term; the dash-dotted line includes the one-body, π-seagull term and pion-in-flight terms and the solid line is for the complete cross-section including contributions from IC.

The missing energy peak for the ^{2}H(e, e′pn) reaction is shown in fig. 7 after correction for random background contributions. The mean of the peak was determined and has a value of 2.1 MeV with a FWHM value of 3.0 MeV. This must be regarded as an upper limit for the resolution of the ^{16}O(e, e′pn) experiment.

5 Results

Figure 6 shows the background-corrected excitation-energy spectrum of the ^{16}O(e, e′pn)^{14}N reaction. The positions of the ground state and the first three low-lying excited states in ^{14}N are marked. There is a prominent peak around the energy expected for the 3.95 MeV (1^+) state in ^{14}N. Given the resolution of the experiment ($\leq$ 3.0 MeV FWHM) this peak will also contain contributions from the 2.31 MeV (0^+) and 7.03 MeV (2^+) excited states if they have been populated. The ^{14}N ground state appears to be at most rather weakly excited.

There is a second strong peak centred at $\approx$ 11 MeV which corresponds to states in the continuum region in the residual ^{14}N nucleus. The width of this peak is such that several states probably contribute and it is not possible to make a reasonable attribution of this peak to any particular states.

The real photon studies of the ^{16}O(γ, pn) reaction [27, 28] also both observed strong excitation of the 3.95 MeV (1^+) state. The study of Isaksson *et al.* [27] observed strong excitation of the ground state (1^+) and of the 7.03 MeV (2^+) state, but neither observed the 2.31 MeV (0^+) state. The photon energies used in both these experiments were somewhat lower than the energy transfer of the present work.

Theoretical calculations of the ^{16}O(e, e′pn) reaction for transitions to the lower-lying states in ^{14}N have been carried out by the Pavia group, see sect. 2.2 and figs. 8 and 9. These calculations predict cross-sections roughly an order of magnitude weaker than observed experimentally, though the relative strength of the different states in ^{14}N is similar to what is seen. The calculations predicted

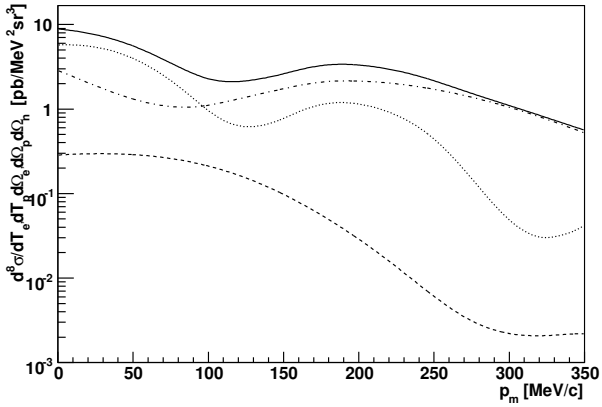

Fig. 9. Theoretical cross-sections from the calculations of the Pavia group [6] for the 2.31 MeV (0^+), 3.95 MeV (1^+), 7.03 (2^+) and the three states combined; represented by the dashed, dotted, dash-dotted and solid lines, respectively. The plots are for the full cross-section including the one-body, π-seagull, pion-in-flight and IC terms.

that transitions to the 3.95 MeV (1^+) state would be the largest which is consistent with the observed missing energy spectrum. Transitions to the 7.03 MeV (2^+) were also predicted to be strong.

DW calculations of the ^{16}O(e, e′pn) reaction, including the effects of MEC, IC, SRC and TC, have also been carried out by the Ghent group for the four low-lying excited states in ^{14}N marked in fig. 6 [44]. The calculations were carried out in the same super-parallel kinematics as the measurement; again these calculations predict cross-sections roughly an order of magnitude smaller than the data. Similarly, to the Pavia calculations these predict that transitions to the 3.95 MeV (1^+) state are strongest; the occupation of the neighbouring excited states is an

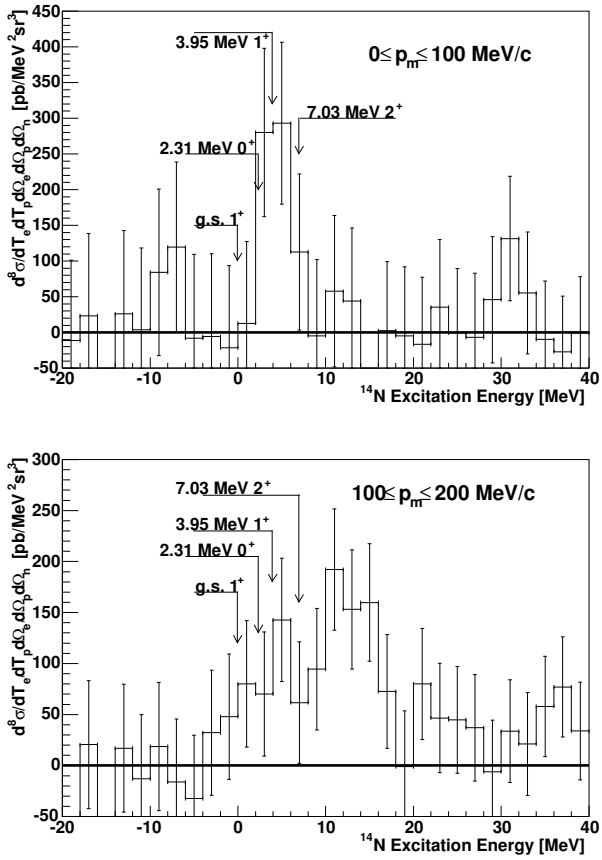

Fig. 10. Excitation energy of the residual ^{14}N nucleus. The top panel shows the excitation energy spectrum for the events in the range $0 \leq p_m \leq 100\,\mathrm{MeV}/c$ while the bottom panel shows the excitation energy spectrum for the events in the range $100 \leq p_m \leq 200\,\mathrm{MeV}/c$.

order of magnitude smaller, which is the same trend as is seen in the data.

Figure 8 shows the measured differential cross-section, as a function of absolute magnitude of the missing momentum, for the group of states from 2 to 9 MeV residual ^{14}N excitation energy. The spectrum has its maximum value at low missing momentum, falls rapidly to around $120\,\mathrm{MeV}/c$ before apparently levelling off and then falling more slowly. The experimental data are compared with the calculations from the Pavia group [6], described in sect. 2.2, which include the sum of contributions of transitions to the 2.31 MeV (0^+), 3.95 MeV (1^+) and 7.03 MeV (2^+) states. Figure 9 shows a comparison of the full cross-sections for transitions to the three different excited states included in the curves of fig. 8. The calculations significantly underestimate the measured cross-section at low missing momenta. Above $100\,\mathrm{MeV}/c$ there is reasonable agreement with the data but the error bars in the data are large. Figure 9 shows that below $100\,\mathrm{MeV}/c$ the main strength is predicted to be from transitions to the 3.95 MeV (1^+) state and above this to the 7.03 MeV (2^+) state.

Figure 8 also shows the cumulative contributions of the Pavia calculations from 1-body, seagull, pion-in-flight

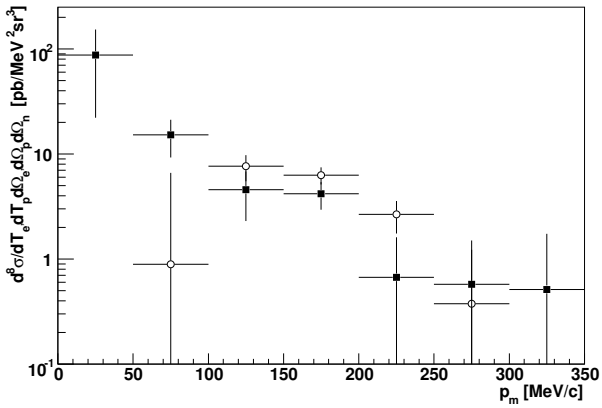

Fig. 11. Comparison of cross-sections of events in the excitation energy range $2 \leq E_x \leq 9\,\mathrm{MeV}$ (squares) and $9 \leq E_x \leq 15\,\mathrm{MeV}$ (circles).

and isobar currents. The largest contribution to the cross-section comes from the isobar currents and in the Pavia calculations the dominant contribution to these are from TCs. The large discrepancy between the experimental and calculated cross-sections and the large statistical errors in the data do not allow strong conclusions to be drawn from the comparison.

The data can be compared with the super-parallel missing momentum spectra observed in the ^{16}O(e, e′pp) reaction [23]. This experiment excited the ground state (0^+) in the residual ^{14}C nucleus and excited states at 7.01 MeV (2^+), 8.32 MeV (2^+), 9.75 MeV (0^+) and 11.3 MeV (1^+). The sum of all the contributions to the different states in the ^{14}C is less than $1.4\,\mathrm{pb\,MeV^{-2}\,sr^{-3}}$. In contrast the summed strength for the group of residual states in ^{14}N for $2 \leq E_x \leq 9\,\mathrm{MeV}$ is ≈ 2 orders of magnitude greater. This ratio is of a similar magnitude to the factor of around 50 seen in the ^{16}O(γ, pp) and (γ, pn) work of ref. [26].

Figure 10 shows the residual ^{14}N excitation spectrum cut into two regions of missing momentum: top: $p_m \leq 100\,\mathrm{MeV}/c$ and bottom: $100 \leq p_m \leq 200$ MeV/c. The group of states from $2 \leq E_x \leq 9\,\mathrm{MeV}$ is present in both missing momentum regions. The excitation energy distribution is somewhat broader and weaker in the higher missing momentum region. This variation in strength supports the idea that the strong 3.95 MeV (1^+) state has its maximum strength at low recoil momentum. Although the statistics are poor, fig. 10 (bottom) also shows apparent strength around 0 MeV which is absent in fig. 10 (top). This may suggest that the ^{14}N ground state has most of its strength in the higher missing momentum region.

The group of higher-energy residual states in ^{14}N have nearly all of their strength in the higher missing momentum range which is similar to what was seen in ref. [45]. In that reference the behaviour was attributed to the dominant states having $L > 0$. Figure 11, which shows the missing momentum dependence of two groups of states, $2 \leq E_x \leq 9\,\mathrm{MeV}$ and $9 \leq E_x \leq 15\,\mathrm{MeV}$, lends further support to this idea. Although for lower missing momentum it is difficult to accurately determine the shape of the

cross-section because of lack of data and poor statistics, it appears that the higher-energy group of states have no strength at zero missing momentum and their distribution peaks at around 150 MeV/c similar to what was seen in ref. [45].

6 Conclusions

This experiment has measured exclusive (e, e′pn) cross-sections for the first time. A large solid-angle array of time-of-flight scintillators was used to detect neutrons and to measure their energies. The energy resolution was good enough to separate groups of states in the residual ^{14}N nucleus, but not individual states. The two groups of states observed were found to have different missing momentum dependencies. Theoretical calculations of the missing momentum spectrum for the low-energy group of states are unable to reproduce the measured strength at low missing momenta.

The authors would like to thank the staff of the Institut für Kernphysik in Mainz for providing the facilities in which this experiment took place. This work was sponsored by UK Engineering and Physical Sciences Research Council and the Deutsche Forschungsgemeinschaft.

References

1. H. Müther, A. Polls, Prog. Part. Nucl. Phys. **45**, 243 (2000).
2. C. Barbieri, W.H. Dickhoff, Prog. Part. Nucl. Phys. **52**, 337 (2004).
3. P. Grabmayr, Prog. Part. Nucl. Phys. **29**, 251 (1992).
4. L. Lapikas, Nucl. Phys. A **553**, 297 (1993).
5. J. Wessling *et al.*, Phys. Rev. C **55**, 2773 (1997).
6. C. Barbieri *et al.*, Phys. Rev. C. **70**, 014606 (2004).
7. C. Giusti *et al.*, Phys. Rev. C **60**, 054608 (1999).
8. C. Giusti, Eur. Phys. J. A **17**, 419 (2003).
9. T. Neff, H. Feldmeier, *Short-range repulsive and tensor correlations in nuclei*, Technical Report, GSI, 2001.
10. J. Levinger, Phys. Rev. **84**, 43 (1951).
11. K. Gottfried, Nucl. Phys. **5**, 557 (1958).
12. S. Boffi *et al.*, *Electromagnetic Response of Atomic Nuclei* (Oxford University Press, 1996).
13. J. Ryckebusch *et al.*, Phys. Rev. C **64**, 044606 (2001).
14. J. Ryckebusch *et al.*, Nucl. Phys. A **624**, 581 (1997).
15. M. Schwamb *et al.*, Eur. Phys. J. A **17**, 7 (2003).
16. M. Schwamb *et al.*, Eur. Phys. J. A **20**, 233 (2004).
17. A. Zondervan *et al.*, Nucl. Phys. A **587**, 697 (1995).
18. L.J.H.M. Kester *et al.*, Phys. Rev. Lett. **74**, 1712 (1995).
19. C.J.G. Onderwater *et al.*, Phys. Rev. Lett. **78**, 4893 (1997).
20. C.J.G. Onderwater *et al.*, Phys. Rev. Lett. **81**, 2213 (1998).
21. R. Starink *et al.*, Phys. Lett. B **474**, 33 (2000).
22. D. Rohe *et al.*, Phys. Rev. Lett. **93**, 182501 (2004).
23. G. Rosner, Prog. Part. Nucl. Phys. **44**, 99 (2000).
24. J. Ryckebusch, W. Van Nespen, Eur. Phys J. A **20**, 435 (2004).
25. D.L. Groep *et al.*, Phys. Rev. C **63**, 014005 (2000).
26. I.J.D. MacGregor *et al.*, Nucl. Phys. A **533**, 269 (1991).
27. L. Isaksson *et al.*, Phys. Rev. Lett. **83**, 3146 (1999).
28. K.R. Garrow *et al.*, Phys. Rev. C. **64**, 064602 (2001).
29. C. Giusti *et al.*, Phys. Rev. C **57**, 1691 (1998).
30. R. Machleidt, Adv. Nucl. Phys. **19**, 1 (1989).
31. H. Herminghaus, Nucl. Instrum. Methods **138**, 1 (1976).
32. N. Voegler *et al.*, Nucl. Instrum. Methods **198**, 293 (1982).
33. S. Sirca, *The axial form factor of the nucleon from coincident pion electro-production at low Q^2*, PhD Thesis, University of Ljubljana, 1999.
34. `http://wwwa1.kph.uni-mainz.de/a1/target.html`.
35. K.I. Blomqvist *et al.*, Nucl. Instrum. Methods Phys. Res. A **403**, 263 (1998).
36. A. Pellegrino *et al.*, Nucl. Instrum. Methods Phys. Res. A **437**, 188 (1999).
37. P. Grabmayr *et al.*, Nucl. Instrum. Methods Phys. Res. A **402**, 85 (1998).
38. R.M. Edelstein *et al.*, Nucl. Instrum. Methods **100**, 355 (1972).
39. R.A. Cecil *et al.*, Nucl. Instrum. Methods **161**, 439 (1979).
40. D. Middleton, *First study of the $(e, e'pn)$ reaction*, PhD Thesis, University of Glasgow, 2003.
41. R.O. Owens, Nucl. Instrum. Methods Phys. Res. A **288**, 574 (1990).
42. M. Distler *et al.*, *Data acquisition and analysis for the 3-spectrometer-setup at MAMI*, in *Proceedings of the 12th IEEE Real Time Congress on Nuclear and Plasma Sciences, 2001*, ISBN 84-699-5463-6.
43. L. Mo, Y. Tsai, Rev. Mod. Phys. **41**, 205 (1969).
44. J. Ryckebusch *et al.*, Phys. Rev. C **61**, 021603 (2000).
45. D.P. Watts *et al.*, Phys. Rev. C **62**, 014616 (2000).